Band tail recombination in polymer:fullerene organic solar cells

Steven A. Hawks, Gang Li, Yang Yang, and Robert A. Street

Articles you may be interested in

Direct and charge transfer state mediated photogeneration in polymer–fullerene bulk heterojunction solar cells
Appl. Phys. Lett. **100**, 193302 (2012); 10.1063/1.4711849

Open-circuit voltage limit caused by recombination through tail states in bulk heterojunction polymer-fullerene solar cells
Appl. Phys. Lett. **96**, 113301 (2010); 10.1063/1.3358121

Thickness dependence of the efficiency of polymer:fullerene bulk heterojunction solar cells
Appl. Phys. Lett. **88**, 243502 (2006); 10.1063/1.2211189

Bimolecular recombination in polymer/fullerene bulk heterojunction solar cells
Appl. Phys. Lett. **88**, 052104 (2006); 10.1063/1.2170424

Light intensity dependence of open-circuit voltage of polymer:fullerene solar cells
Appl. Phys. Lett. **86**, 123509 (2005); 10.1063/1.1889240

Band tail recombination in polymer:fullerene organic solar cells

Steven A. Hawks,[1,2] Gang Li,[2] Yang Yang,[2] and Robert A. Street[1,a)]

[1]*Palo Alto Research Center, 3333 Coyote Hill Road, Palo Alto, California 94304, USA*
[2]*Department of Materials Science and Engineering, University of California Los Angeles, California 90095, USA*

Recombination through band tail localized states is studied analytically and by measurement of the forward-bias dark current as a function of temperature in three different organic bulk-heterojunction solar cells. The Shockley-Read-Hall mechanism is analyzed for the specific case of recombination between mobile carriers and an exponential distribution of localized band tail states. The analysis gives a simple relation between the dark current ideality factor and the band tail slope. Assumptions of the model are verified by numerical drift-diffusion modeling. Diode current-voltage measurements give good agreement with the analytical model, confirming that the band tail recombination mechanism applies to at least some organic solar cells. Deep traps provide a secondary recombination channel in some devices. © 2014 AIP Publishing LLC.
[http://dx.doi.org/10.1063/1.4892869]

I. INTRODUCTION

Organic bulk heterojunction (BHJ) solar cells based on polymer:fullerene blends have increased rapidly in efficiency due to the introduction of optimized new materials and the improvement of device architecture.[1–4] Present devices are largely limited by the compromise between optical absorption and fill factor.[5] Thicker devices typically absorb more of the incident light but also have increased recombination due to the need to collect charge over a longer distance and at a lower internal electric field. It is therefore important to reduce the recombination to achieve higher efficiency, and hence it is important to understand the recombination processes in detail. Several recombination mechanisms have been studied in BHJ devices, including geminate and Langevin recombination, as well as recombination through localized (trap) states.[4] Since BHJ cells use disordered materials, there is a strong theoretical expectation and significant experimental evidence for the presence of localized band-tail states. Thus, it is reasonable to expect that band tail states also play a significant role in the recombination of mobile carriers.

Along these lines, this paper aims to develop and test a recombination model for the forward-bias dark current in BHJ solar cells based on an exponential distribution of localized band-tail states and the Shockley-Read-Hall mechanism. We demonstrate the validity of the model by analyzing the dark diode ideality factor as a function of temperature in several different BHJ materials systems. The photocurrent spectral response (PSR) as well as numerical drift-diffusion modeling are used to verify the model predictions.

II. THE DARK DIODE CURRENT IDEALITY FACTOR

The dark diode current in low forward bias is characterized by an exponential dependence on voltage (V) that goes like $\exp(qV/n_{id}kT)$ with an ideality factor n_{id}. The exponential region corresponds to small current-density values where the magnitude of the drift and diffusion components in the recombination zone outweighs the total current, which minimizes the influence of transport and contact effects. The diode ideality factor is characteristic of the recombination mechanism. For the classic models, band-to-band or Schottky contact recombination gives $n_{id} = 1$, while Shockley-Read-Hall (SRH) recombination through midgap traps gives $n_{id} = 2$.[6–8]

Most BHJ solar cells have room temperature ideality factors measured by the dark diode current of ~1.3–2,[9–12] and so the associated recombination mechanisms are not immediately apparent. Several papers attribute this intermediate ideality factor to the presence of a distribution of localized states, including band-tail states,[13–15] but a direct experimental connection between n_{id} and the measured band-tail slope has not been fully explored. Some experimental data already suggest the importance of band-tail recombination and even correlate the ideality factor with the band-tail slope.[16] However, the ideality factor is also influenced by the presence of other deep states that provide a separate recombination channel. For instance, the ideality factor increases when deep traps are induced by exposure to radiation in both poly[carbazole-dithienyl-benzothiadiazole]:phenyl-C_{61}-butyric acid methyl ester (PCDTBT:PCBM) and poly(3-hexyl thiophene) (P3HT):PCBM solar cells.[17] Hence, the ideality factor may reflect more than one recombination mechanism, and the dominant mechanism may depend on the specific material and device condition. The ideality factor can also be obtained from the light intensity dependence of the open-circuit voltage (V_{OC}). Reports of this measurement in organic BHJ solar cells have included discussion of whether the dark and illuminated ideality factors are the same or different.[9,12]

The ideality factor can also be measured in single carrier devices. In such structures, bulk electron-hole recombination is excluded so that the ideality factor will therefore generally be different, and is usually associated with the Schottky

a)Author to whom correspondence should be addressed. Electronic mail: street@parc.com.

contact.[9] Single carrier devices also exhibit pronounced space charge limited current transport.

There have been various attempts to model the ideality factor of organic diodes. This can be done by solving the drift-diffusion equations with assumed recombination mechanisms and contact boundary conditions.[13,15] Early calculations of current-voltage behavior assume either geminate or Langevin-type recombination and have generally neglected the presence of band-tail states.[18–22] Giebink *et al.*[23] give an analytical model for the dark forward current, including the presence of band-tail states, but the analysis is for a planar heterojunction diode rather than a BHJ structure. The first analysis of the dark current ideality factor which assumed an exponential band-tail density of states $\exp(E/E_0)$ was by van Berkel *et al.*[24] and gave for the ideality factor,

$$\frac{1}{n_{id}} = \frac{1}{2} + \frac{kT}{2E_0}. \tag{1}$$

Various authors have recently derived or used the same or a similar relation in the context of organic bulk-heterojunction solar cells.[13–15] However, we show that Eq. (1) fails to account for thermal emission from traps.

Section III describes a revised Shockley-Read-Hall based analysis of band tail recombination and shows how including thermal emission from traps leads to a significantly different equation for the ideality factor than Eq. (1). Sections IV and V detail our measurements of the ideality factor through both dark *I-V* and illuminated V_{OC} vs. light intensity measurements, and the band-tail slope by the photo-current spectral response (PSR) technique.[25] The results of these measurements as well as numerical drift-diffusion simulations are discussed in Sec. VI.

III. SHOCKLEY-READ-HALL ANALYSIS OF BAND TAIL RECOMBINATION

The assumed BHJ cell energy band structure is shown schematically in Figure 1. Electrons are injected from the cathode and move in the fullerene lowest unoccupied molecular orbital (LUMO), holes are injected from the anode and move in the polymer highest occupied molecular orbital
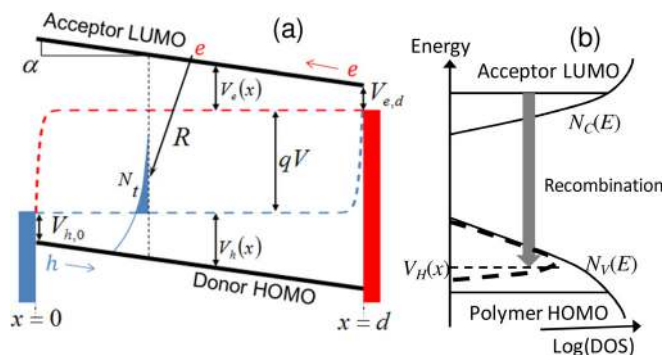

FIG. 1. (a) Band diagram for the BHJ cell under forward bias, showing the quasi-Fermi energies (dashed lines) and various parameters. (b) The assumed density of states distribution with an exponential distribution of band-tail states. The equilibrium trapped hole concentration which peaks at the qFE is indicated.

(HOMO), and recombination occurs at the distributed interface between the polymer and fullerene domains. The presence of localized band-tail states is well documented, and current flow in disordered semiconductors is generally described in terms of a transport energy that separates mobile states and localized band-tail states.[10,13,25,34] In forward bias, the occupancy of states by electrons and holes are described by quasi-Fermi energies (qFE), which are indicated along with the various parameters in the figure. Figure 1(b) shows the density of states with exponential band tails.

The Shockley-Read-Hall (SRH) mechanism[6,7] assumes capture and thermal emission of electrons and holes through trap states with a state density N_t at a trap energy E_t, leading to a recombination rate,

$$R = \frac{C_n C_p (np - n_i^2)}{C_n(n + N_C \exp(-E_1/kT)) + C_p(p + N_V \exp(-E_2/kT))} N_t, \tag{2}$$

where n and p are the mobile electron and hole concentrations, E_1 and E_2 are the energetic distance between the trap energy and the LUMO and HOMO transport energies, respectively, and the n_i^2 term is from thermal generation. N_C and N_V are the effective density of states at the LUMO and HOMO transport energies and C_n and C_p are the capture rate constants. For definiteness, the model assumes a broader exponential band tail on the HOMO with slope E_0 and a narrower band tail on the LUMO, which is probably the situation in most BHJ cells. The opposite situation in which the LUMO band tail is broader than the HOMO band tail will give an equivalent result.

There are three main recombination transitions to consider: between mobile states at or above the transport energy, between a mobile state and a localized band-tail state, and between two localized band-tail states. Recombination between localized states has a very low probability because the states are physically separated and can only recombine by tunneling, and at the typical electron and hole densities ($\sim 10^{16}\,\mathrm{cm}^{-3}$) the average separation is large and hence the tunneling probability is very small. When $E_0 > kT$ for the wider band tail, the majority of carriers are in the band tail rather than being in mobile states, and the ratio can be 100–1000, which is also related to the ratio of the free and trap-limited mobility. Hence, we expect that recombination from a mobile state in the fullerene LUMO to a localized band-tail state in the polymer HOMO is much more probable than transitions between mobile states, and thus this is the mechanism we analyze. Several others have reached the same conclusion for organic BHJ devices and other diodes.[13,14,26] All of the possible recombination transitions in the BHJ cell are between an electron in the fullerene and a hole in the polymer and so necessarily involve a tunneling component across the interface.

Analysis of the SRH mechanism usually makes a simplifying assumption that the energy level(s) of the recombination centers either lie between the quasi-Fermi energies or outside of them. In many situations, the relative energy of the qFE and the recombination center can change with the illumination intensity and temperature, etc. For recombination

centers lying between the qFEs where thermal emission is negligible, the recombination rate simplifies to,

$$R = \frac{C_n C_p np}{C_n n + C_p p} N_t. \tag{3}$$

The band tail recombination model presents an unusual situation for the SRH analysis. As shown in Fig. 1(b), the population of trapped holes, which are herein the presumed recombination centers, peaks at the qFE because the hole density drops off at higher energy due to the band tail density of states and falls off at low energy due to the Fermi function. Hence neither of the usual simplifying assumptions applies since the recombination centers are at, or very close to, the qFE. Furthermore, provided that the qFE stays within the band tail distribution, the recombination centers remain at the qFE, independent of temperature, light intensity, and position in the device.

In terms of the SRH equation (Eq. (2)), our model assumes that E_1 is large enough that thermal excitation of electrons is negligible, while E_2 is small enough that the trapped holes are in thermal equilibrium with the mobile holes. The validity of these assumptions is discussed in Sec. V. For the band diagram and the parameters shown in Fig. 1(a), the mobile electron n and hole p concentrations as a function of position x and applied bias are,

$$n = N_C \exp\left(-\frac{qV_e(x)}{kT}\right); \quad p = N_V \exp\left(-\frac{qV_h(x)}{kT}\right). \tag{4}$$

$V_h(x)$ and $V_e(x)$ are the separation of the qFE and the HOMO and LUMO band edges as a function of position. The density of recombination centers $N_t(x)$ is approximated to the density of states in the exponential band-tail states above the quasi-Fermi energy (assuming a low temperature Fermi function),

$$N_t(x) = N_V \exp\left(-\frac{qV_h(x)}{E_0}\right). \tag{5}$$

By straightforward kinetics, the total electron recombination rate is the product of the electron density, the hole trap density, and the recombination rate constant, integrated across the device,

$$R = \int_0^d C_n n(x) N_t(x) dx$$
$$= C_n N_C N_V \int_0^d \exp\left(-\frac{V_e(x)}{kT}\right) \exp\left(-\frac{V_h(x)}{E_0}\right) dx. \tag{6}$$

Assuming a linear band profile for the cell of thickness d,

$$V_h(x) = V_{h0} + \alpha x; \quad V_e(x) = V_{e0} + \alpha(d - x) \tag{7}$$

then,

$$R = C_n N_C N_V \exp\left(-\frac{V_{e0}}{kT}\right)$$
$$\times \exp\left(-\frac{V_{h0} + \alpha d}{E_0}\right) \int_0^d \exp\left(-\alpha(d-x)\left(\frac{1}{kT} - \frac{1}{E_0}\right)\right) dx. \tag{8}$$

Since E_0 is larger than kT, the exponent in the integral is negative and has its largest value when $x = d$, so that most of the current flows on the cathode side of the cell. Equation (7) and the parameters in Fig. 1(a) give,

$$V_{e0} + V_{h0} + \alpha d + qV = E_G; \quad V_{h0} + \alpha d = E_G - V_{e0} - qV, \tag{9}$$

where E_G is the interface band gap between the polymer HOMO and the fullerene LUMO. The built-in potential is $qV_{BI} = E_G - V_{e0} - V_{h0}$, and thus $\alpha d = q(V_{BI} - V)$. V_{e0} and V_{h0} are the energy barriers at the electron and hole contacts, respectively. The dark current is the excess integrated recombination rate relative to $V = 0$,

$$J_D(V) = \beta q d C_n N_C N_V \exp\left(-\frac{V_{e0}}{kT}\right)$$
$$\times \exp\left(-\frac{E_G - V_{e0}}{E_0}\right) \left[\exp\left(\frac{qV}{E_0}\right) - 1\right]. \tag{10}$$

The dimensionless parameter β is,

$$\beta = s\left[1 - \exp\left(-\frac{1}{s}\right)\right]; \quad s = \frac{1}{q(V_{BI} - V)}\frac{E_0 kT}{E_0 - kT}, \tag{11}$$

and the ideality factor for this model is from Eq. (10),

$$n_{id} = \frac{E_0}{kT}. \tag{12}$$

The model therefore predicts that the slope of the diode region of the dark current is independent of temperature (apart from any temperature dependence of E_0) and that $n_{id}kT$ is equal to the band-tail slope.

Equation (12) is manifestly different from Eq. (1), which was also obtained from SRH analysis of a similar situation. The difference is that Eq. (1) used the approximation of Eq. (3) that the recombination centers are between the qFEs and hence neglects thermal emission. A consequence is that the dominant recombination traffic is forced to be at the center of the device $x = d/2$ where $n \approx p$, and with this added condition, Eq. (1) follows from Eqs. (4) and (5). However, Eq. (3) is not appropriate for band tail recombination since the active traps are at the qFE, as discussed above. Equation (3) omits the SRH term governing the thermal population of the recombination centers, but the assumption of a flat qFE requires a thermal equilibrium hole population. Equations (10) and (12) result when recombination is allowed to be throughout the device and the analysis shows that the dominant recombination is closer to the cathode rather than in the center of the device. Tzabari and Tessler also discuss the need to include the thermal excitation terms in Eq. (2) for the case of shallow hole traps.[27]

Under some experimental conditions, the qFE might not be flat across the device, and in particular the hole qFE will move up near the cathode if the recombination traffic is such that hole thermal equilibrium cannot be maintained across the device, for example, from transport limitations. In this case, the maximum current is at $x < d$. The dependence of current on voltage for this case is obtained by evaluating the

integrand in Eq. (6) for an arbitrary value of x and using Eqs. (7) and (9) to derive the exponential voltage dependence. This calculation leads to,

$$\frac{1}{n_{id}} = 1 - \frac{x}{d}\left(1 - \frac{kT}{E_0}\right), \tag{13}$$

which reduces to Eq. (1) for $x = d/2$ and Eq. (12) for $x = d$.

An exponential band tail is well known to result in dispersive transport, characterized by a dispersion parameter $\alpha_{tr} = kT/E_0$. Hence an interesting relation is that when charge transport and recombination both arise from the band tail states, then $n_{id}\alpha_{tr} = 1$.

IV. EXPERIMENTAL RESULTS

A. Experimental methods

Three different well-performing BHJ solar cells were used in these studies. P3HT:PCBM and PBDTT-DPP:[28]PCBM cells were fabricated at UCLA, and PCDTBT:PCBM devices were made at UC Santa Barbara. The details of the device fabrication are described elsewhere.[29–31] The P3HT:PCBM cell fabrication used the solvent annealing approach, which gives a high degree of polymer crystallinity. Measurement of the steady-state dark current was made with the devices mounted in an evacuated variable-temperature cryostat and measured by a Keithley 6487 picoammeter. The PSR measurement was made with a monochromatic light source using lock-in amplifier techniques as described elsewhere.[16,25] The PSR signal is normalized to the power of the incident light. The light intensity dependence of the open-circuit voltage was made with a white light emitting diode module (Helieon 1200 lm), using a silicon photodiode and a Keithley 6487 picoammeter to monitor the light intensity. To minimize heating, the devices were only illuminated for ~1–2 s at each light intensity.

B. Experimental measurements

Figure 2 shows examples of the dark forward bias current-voltage $J_D(V)$ characteristics for the three different polymer:PCBM blends at temperatures between ~180 and 330 K. The slope of the exponential region of the diode current is evidently not strongly temperature dependent and hence the ideality factor changes with temperature, contrary to predictions by the classic models of the diode dark current. The ideality factor was extracted by two methods: the first method was from fits to the dark diode equation,

$$J_D(V) = J_0 \exp\left[\frac{q(V - J_D(V)R_S)}{n_{id}kT} - 1\right] + \frac{V - J_D(V)R_S}{R_P}, \tag{14}$$

where R_S is the series resistance and R_P is the parallel shunt resistance. The fit is performed by using measured values of $J_D(V)$ to evaluate the right hand side of Eq. (14). The lines in Fig. 2 are fits to this equation. The second method was from the function,
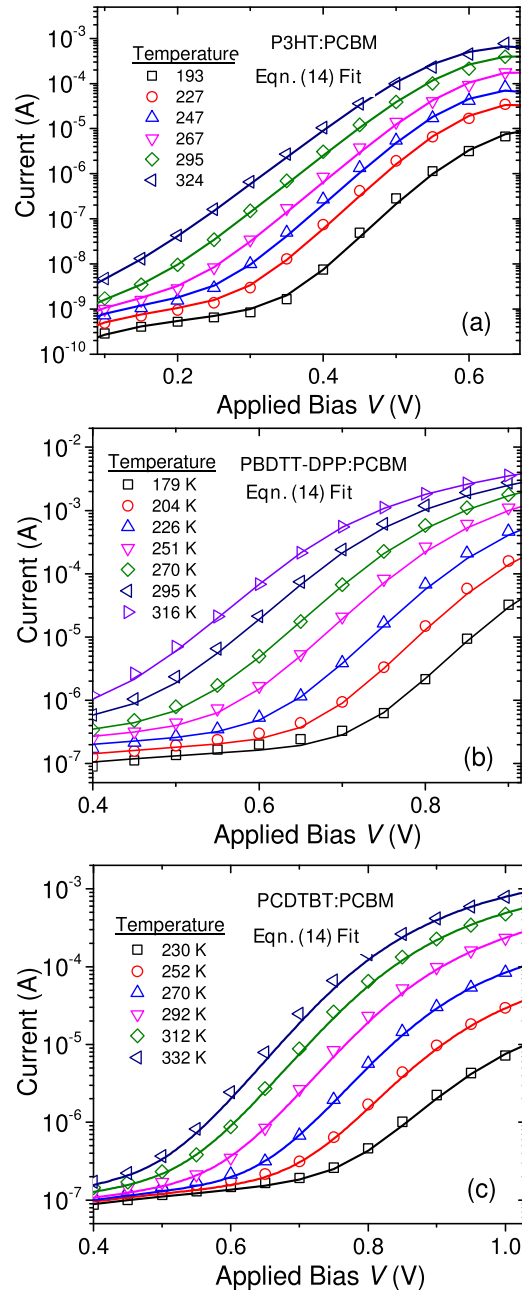

FIG. 2. Dark current voltage characteristics at various temperatures as indicated, for the three different BHJ solar cells (a) P3HT:PCBM (b) PBDTT-DPP:PCBM (c) PCDTBT:PCBM. The points are data and the solid lines are fits to the diode equation Eq. (14).

$$n_{id}kT = q \min\left(\frac{dV}{d\ln(J_D(V))}\right), \tag{15}$$

which is from the steepest slope of the exponential region in a semi-log plot. The $J_D(V)$ data show typical series and shunt resistances, although the shunt resistance for the P3HT:PCBM cell was particularly high and so the exponential region extends over a larger voltage range. The P3HT:PCBM series resistance was not accurately ohmic and probably includes a significant space-charge limited current or other non-Ohmic contributions,[32] thus the data were only fitted over a limited voltage range over the series-resistance region.

The exponential slope factor $n_{id}kT$ is shown in Fig. 3 as a function of temperature. The data for P3HT:PCBM and PBDTT-DPP:PCBM show both methods of extraction from Eqs. (14) and (15), and the results differ by no more than 2 meV, which is roughly the uncertainty in the fit to Eq. (14). The PCDTBT:PCBM data show results from two different samples. The values of $n_{id}kT$ are weakly dependent on temperature, increasing slightly for P3HT:PCBM and PBDTT-DPP:PCBM, and either flat or decreasing for PCDTBT:PCBM. Others have also reported polymer:fullerene current-voltage characteristics that, by inspection, have weakly temperature dependent values of $n_{id}kT$.[11,33] Hence, it is more appropriate to examine the actual slope factor $n_{id}kT$ rather than n_{id} alone.

An independent measurement of the band-tail slope is needed to evaluate the recombination model. Several experiments have provided estimates of the slope of the band tail in BHJ cells, but the resulting values are widely varying.[14,25,34–36] We use the photocurrent spectral response (PSR) technique, which measures the optical absorption of excitations that generate photocurrent, including bulk exciton absorption, charge-transfer absorption, and localized-state transitions.[25,37] There is significant precedent for the use of a PSR-like technique to characterize the sub-gap electronic structure of inorganic amorphous solids.[38–40] In bulk-heterojunction organics, we typically observe a PSR that has an exponential slope at energies below the charge transfer (CT) band gap, which we have interpreted as corresponding to the slope of the wider band tail.[25] Experimental evidence for this interpretation of the PSR exponential slope is that the same value of band-tail slope is deduced from transient photocurrent measurements in P3HT:PCBM and PCDTBT:PCBM using a dispersive transport model.[25,34] The CT absorption may be broadened to a slightly larger value than E_0 by the convolution of the valence band and conduction band density of states and may also be broadened by electron-phonon coupling. However, we foresee no

mechanism by which the CT absorption measured by PSR can have an exponential slope that is substantially steeper than the wider of the two band tails.

Room temperature PSR data are shown for the three devices in Fig. 4 and the temperature dependence of the exponential band-tail slope for P3HT:PCBM is shown in the inset. The arrows show the approximate energy of the CT band gap E_G and there is a region of exponential absorption at lower energy. The room temperature PSR band-tail slopes are $E_0 = 32$, 27, and 47 meV, respectively, for P3HT:PCBM, PBDTT-DPP:PCBM and PCDTBT:PCBM. The PCDTBT:PCBM and PBDTT-DPP:PCBM PSR spectra have a clear change of slope at low absorption, suggesting the presence of other deep trap states, but P3HT:PCBM has a more extended exponential region. The band-tail slope of P3HT:PCBM shows a small temperature dependence of E_0, which is also comparable to the temperature dependence of $n_{id}kT$. The band tail state distribution may have some thermal broadening which can explain the observed weak temperature dependence of the slope.

Figure 5 shows the complete fit of the SRH model Eq. (10) to the $J_D(V)$ data for the three solar cells, including the series and shunt resistance. The analysis is only valid up to the built-in potential, and this is the voltage range of the fit. The fit assumes that E_0 has a small linear temperature dependence, as indicated by the n_{id} data of Fig. 3 and consistent with the PSR data of Fig. 4, rather than using independent fit parameters of E_0 for each data set. Figure 6 compares the temperature dependence of the fit parameters for E_0 ($= n_{id}kT$) from Eq. (10) to the measured E_0 from the PSR data. The fit values of E_0 for P3HT:PCBM increase from 31 meV to 36 meV across the temperature range which agrees closely with E_0 measured by PSR. These values are larger than the $n_{id}kT$ values obtained from the fit to the diode equation (Fig. 3) by about 3 meV. The reason for this small difference is that the β prefactor to Eq. (10) contains terms with both T and V and hence slightly changes the slope of the exponential region compared to the diode equation. The data can also be fit slightly less well with a temperature-
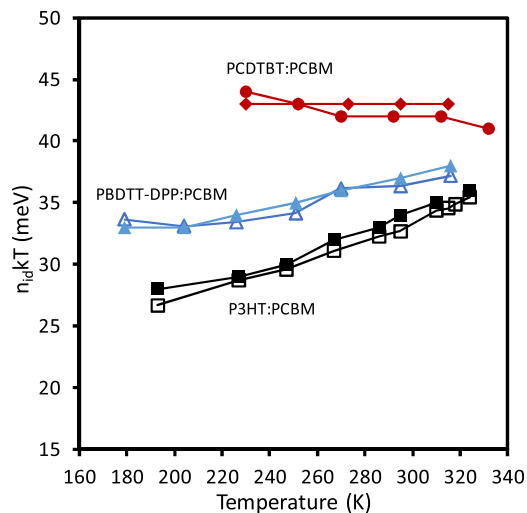

FIG. 3. Measured values of $n_{id}kT$ for the three solar cells in Fig. 2. The P3HT:PCBM and PBDTT-DPP:PCBM data show values obtained from the fit to Eq. (14) (filled symbols) and from Eq. (15) (open symbols). The PCDTBT:PCBM data is for two different samples using Eq. (14) (filled diamonds and circles).
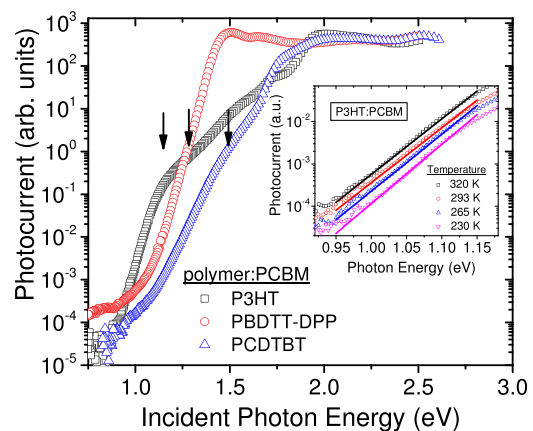

FIG. 4. Photocurrent spectral response measurements for the three different solar cells. The arrows indicate the approximate location of the charge transfer band gap E_G and the band-tail slope is measured from exponential region at lower energy. The inset shows the exponential region for P3HT:PCBM at different temperatures (data are offset vertically for clarity).
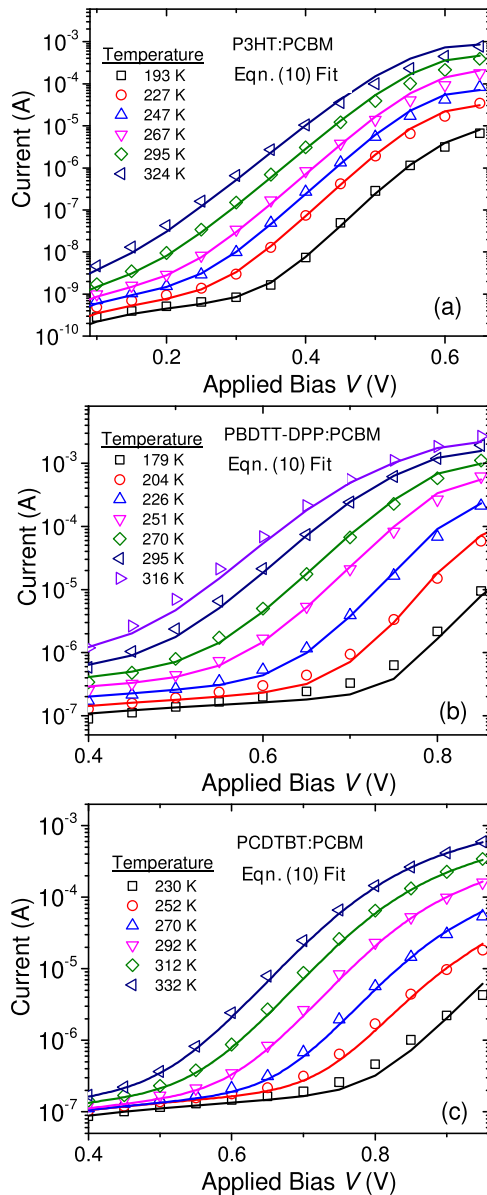
FIG. 5. Dark current data from Fig. 2 (points) and the fit to the SRH model Eq. 10 (lines) for the three types of solar cell (a) P3HT:PCBM (b) PBDTT-DPP:PCBM (c) PCDTBT:PCBM.
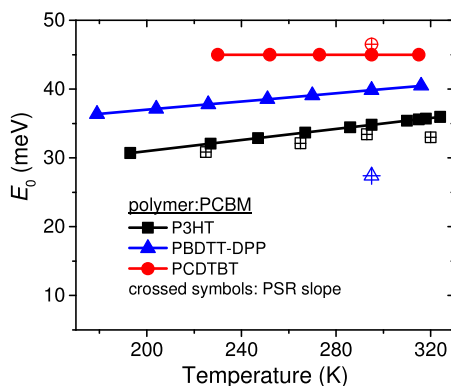

FIG. 6. Plot of parameter values of $E_0 = n_{id}kT$ (filled points and lines) obtained from the Eq. (10) fit to the data in Figure 5, compared to the band-tail slope values measured by PSR (crossed open symbols) for the three solar cells.

independent value of E_0. The PBDTT-DPP:PCBM data assume the same temperature dependence of E_0 as for the dark ideality factor, while the PCDTBT:PCBM is fitted with a constant E_0, as indicated by the data in Fig. 3. The PCDTBT:PCBM band tail slope may have some temperature dependence,[10] but we chose to fit the data with the temperature dependence in Fig. 3 for consistency and so as not to introduce another parameter. The fit values of E_0 are also larger than the $n_{id}kT$ values in Fig. 3 by 2–3 meV for the same reason.

C. Ideality factor measured from the open circuit voltage

The solar cell current can be defined as the sum of the dark current and the photocurrent J_{PC}, where J_{PC} is the difference in the measured current under light and dark conditions.[41] Since the current at V_{OC} is zero, it follows that for an ideal exponential diode-dark current without shunt resistance that J_{PC} and V_{OC} are related by

$$V_{OC} = \frac{n_{id}kT}{q} \ln\left(\frac{J_{PC}(V_{OC})}{J_0} + 1\right)$$

$$\cong const + \frac{n_{id}kT}{q}\ln(Gf(V_{OC})). \quad (16)$$

The second expression arises because $J_{PC} \gg J_0$ and the reverse bias photocurrent is linear in light intensity G when all the photo-generated charge is collected. The voltage dependent term denoted by $f(V)$ represents the voltage dependence of J_{PC} and reflects the shape of the cell fill factor and all non-ideal processes occurring in the cell.[10] In a high fill factor cell, $f(V)$ is constant up to near the built-in potential, but in a low fill factor cell, $f(V)$ will change more rapidly. Hence, the light intensity of V_{OC} is an alternative measurement of the dark ideality factor, but with the benefit that the series resistance does not affect Eq. (16) because no external current flows.[12] The shunt resistance, however, does affect Eq. (16) and V_{OC} is given by $R_P Gf(V_{OC})$ in the region dominated by the shunt resistance.

The open-circuit voltage as a function of incident light intensity is shown in Figure 7 for the same devices as for the dark current in Figure 2. The strong drop in V_{OC} at low light intensities in Figure 7 is due to the shunt resistance as described above. At high light intensity, the slope of V_{OC} vs. $\ln(G)$ flattens off because the $f(V_{OC})$ term in Eq. (16) decreases as V_{OC} increases. The photocurrent drops to zero (and changes sign) at the built-in potential so that $f(V_{BI}) = 0$ and therefore V_{OC} is limited to being less than V_{BI}. The flattening of V_{OC} at high light intensity may also have a small contribution from sample heating by the strong illumination because V_{OC} decreases at higher temperature. The built-in potential is indicated in Figure 7 and is measured by the voltage at which the cell photocurrent tends to zero, obtained by fitting the voltage dependence of the photocurrent to a simple recombination model.[16] The observed flattening off of V_{OC} at high illumination is consistent with the measured V_{BI} and is independent of the specific recombination mechanism because in principle $f(V)$ can arise from any mechanism.
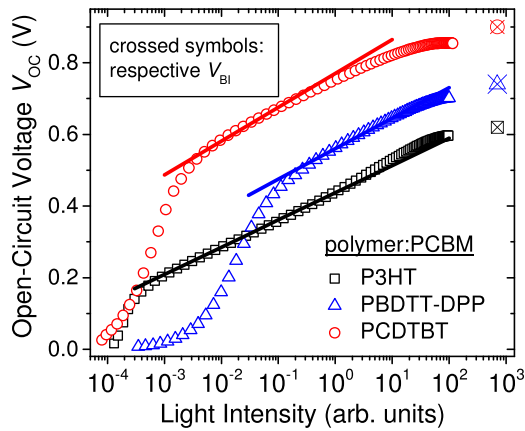
FIG. 7. The dependence of V_{OC} on incident light intensity for the three different cells. The strong drop in V_{OC} at low light intensity arises from the shunt resistance. The solid lines are the slopes corresponding to the measured dark ideality factors.

Alternative descriptions of this effect based upon surface recombination dominating at high V_{OC} values have also been given in the literature.[12] The solid lines in Figure 7 are slopes corresponding to the measured room temperature dark-current ideality factor, adjusted vertically to match the V_{OC} data. The data show that the dark and light ideality factors agree well over much of the expected range. The P3HT:PCBM data show some curvature with an apparently larger ideality factor at high voltage, which is discussed further below. The decrease in V_{OC} due to the $f(V)$ factor is most evident in the PCDTBT:PCBM data.

V. DISCUSSION

Figure 6 compares the $n_{id}kT$ values from the fit of the data to Eq. (10) with the measured E_0 data from PSR. The P3HT:PCBM and PCDTBT:PCBM data show almost perfect agreement with the fit values of $n_{id}kT$ within 2 meV of the measured band-tail slope. The data therefore show that Eq. (12) gives almost perfect agreement for P3HT:PCBM and PCDTBT:PCBM but is a less good fit for PBDTT-DPP:PCBM where E_0 is 27 meV compared to $n_{id}kT$ of 39 meV at room temperature, which is discussed further below. In addition, the model agrees with data for hydrogenated amorphous silicon, since the predicted slope for $n_{id} \sim 1.5$ at room temperature is $E_0 \sim 38$ meV, which is in good agreement with the measured band tail slope and with the hole mobility dispersion parameter of ~ 0.6.[42] The agreement with the data strongly indicates that the band tail recombination mechanism dominates in the corresponding materials.

The fits to the data in Fig. 5 assume values of N_C and N_V of 10^{20} cm^{-3}, and adjusts V_{e0} and C_n. We assume an average value of V_{BI} based on the measured value at room temperature, although V_{BI} likely does vary with temperature.[43] The extracted value of V_{e0} is 0.11 V, 0.28 V and 0.44 V for P3HT:PCBM, PBDTT-DPP:PCBM and PCDTBT:PCBM, respectively, and the value of C_n is 4×10^{-10} cm^3/s, 1.8×10^{-8} cm^3/s, and 7×10^{-7} cm^3/s for the three materials. Both parameters are sensitive to the temperature dependence of E_0, where reducing the temperature dependence of E_0

increases V_{e0}. The P3HT:PCBM value of V_{e0} is perhaps lower than expected but V_{e0} is itself probably temperature dependent, and the use of contact barrier heights of 0.1 eV or less have been used by others in drift-diffusion modeling to describe various aspects of these cells.[12,20,44] C_n is the product of the capture cross section and the thermal velocity and the fit values are consistent with an atomic scale cross-section of about 10^{-15}–10^{-14} cm^2 and a thermal velocity of $\sim 10^6$ cm/s. Given all the uncertainties in the values, we cannot deduce any parameter with accuracy, but the values are at least consistent with general expectations.

The observation of a significant difference between E_0 and $n_{id}kT$ for PBDTT-DPP:PCBM suggests that another mechanism may be involved, and we propose that this is the added contribution of deeper band-tail states. The PSR data of Fig. 4 show a change of slope at about 1.1 eV, indicating that there is a substantial density of deep states. More significantly, this change of slope occurs only about 0.2 eV below the CT band gap and so the broader band of deep states will intersect the hole qFE at relatively high applied voltage, which could therefore easily explain the relatively larger $n_{id}kT$. There is a similar change of slope in the PSR data of PCDTBT:PCBM, but this occurs further from the CT band gap and so will have less influence on the value of $n_{id}kT$ in the observable voltage range. PSR measurements in PCDTBT:PCBM and P3HT:PCBM find that these deep states increase in density as a result of prolonged illumination and they are attributed to defects resulting from C-H bond-breaking.[17] It is not yet known if the deep states in pristine samples are of a similar type. A more detailed analysis is needed to calculate the effect on $n_{id}kT$ of these deeper states.

An increase of the ideality factor by the presence of a sufficiently high density of deep states is known from studies of x-ray and light-induced degradation of BHJ cells.[16,17] Figure 8 shows that the ideality factor in PCDTBT:PCBM increases from ~ 1.7 to above 3 as the density of induced deep states increases as a result of prolonged exposure to light[16] and there is a similar increase in P3HT:PCBM.[17] The relative deep state density is evaluated from the solar cell current-voltage characteristics using a charge collection
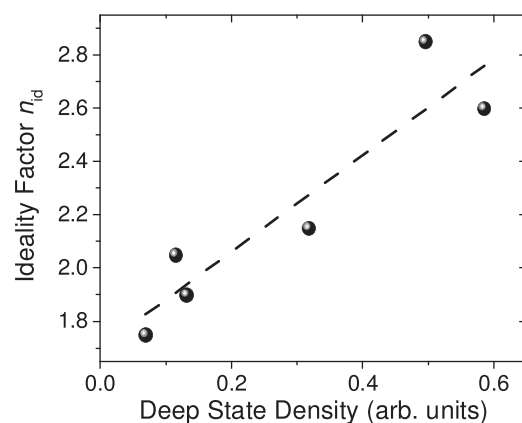

FIG. 8. Increase of the ideality factor in PCDTBT:PCBM with deep state density induced by prolonged illumination. The data are re-plotted from Ref. 16.

model.[10] Some BHJ cells, notably MEHPPV:PCBM have an ideality factor that is independent of temperature and closer to unity.[9] These properties indicate that a different recombination mechanism dominates, which could be geminate recombination or recombination at a contact. We emphasize that several different recombination mechanisms are possible in BHJ cells and the dominant process will depend on the specific material and the device structure.

The measured ideality factor can also be influenced by extrinsic effects. Some forms of contact resistance associated with ambient degradation have an exponential current-voltage relation and lead to an apparent increase in the ideality factor.[32] In a similar regard, the differences in the dark and light ideality factor commonly observed in polymer:fullerene solar cells can also be easily caused by errors in interpretation due to resistive-type effects.[9,12] The data in Figure 7 indicate that the measured ideality factors are essentially identical in the dark and under illumination. Equation (16) shows that the dark and illuminated ideality factors must be the same apart from the $f(V)$ term. The agreement does not imply that the recombination mechanisms in the dark and under illumination are the same but only that $f(V)$ is relatively constant over the range of voltages measured. Hence cells with high fill factor will show the same ideality factor, while those with low fill factor will exhibit a difference due to the change in $f(V)$. There is, however, a strong expectation and ample evidence that the recombination mechanisms are the same in the dark and under illumination. The cell fill factor reflects the recombination under illumination and decreases with both an increase in band-tail slope and an increase in deep state density and is correlated with the changes in dark ideality factor.[16,17]

A. Validity of the model

The analysis that leads to Eq. (10) assumes that the quasi-Fermi energy is flat across the cell and that the bands are linear. In terms of the SRH equation, (Eq. (2)) one important condition for validity of the model is that the thermal excitation rate between the band tail and HOMO transport energy is large enough to maintain the flat qFE. When the electron traps are sufficiently far from the LUMO band that there is little thermal excitation back to the LUMO, the SRH equation can be expressed as,

$$R = C_n n N_T \left[\frac{1}{1 + \exp\left(-(E_t - E_F)/kT\right) + C_n n / C_p p} \right], \quad (17)$$

where E_t is the trap energy. This equation corresponds to the assumed model apart from the $C_n n / C_p p$ term when summed over the distribution of band-tail states. The first two terms in the denominator in brackets are the Fermi-Dirac function, which is the assumed trap occupancy function. Hence the model is valid provided that $C_n n / C_p p < 1$.

This condition for validity of the model is easily met when the applied voltage is close to the built-in potential when $p \approx n$, and is increasingly hard to meet at lower voltages when $p \ll n$ and the model is only valid when $C_n \ll C_p$. There are, however, good reasons why $C_n \ll C_p$ in a BHJ

solar cell. First, the electron is making a transition from the fullerene to the polymer, which involves a tunneling term of the form $\exp(-2R/R_0)$ where R is the separation of the electron from the hole band tail state and R_0 is the electron wave-function penetration into the polymer. Not much is known about the parameters R or R_0, but the exponential term can easily reduce the capture rate by a few orders of magnitude. The hole capture transition is higher because the band-tail states are in the polymer and no tunneling by holes is involved. Second, the electron transition is across a substantial fraction of the interface band gap energy, while the hole transition to the band-tail state is over a much smaller energy. In general, the transition rate decreases as the energy difference between the initial and final state increases. Hence there is good reason to expect that $C_n \ll C_p$ and that the model is valid over a reasonable voltage range. Additionally, there is precedent in the literature for using highly asymmetric recombination coefficients when modeling the optoelectronic properties of these devices.[12,13,15,36,45] Eventually, at a low enough applied voltage, p is so much smaller than n that the model will break down. However, the exponential region of the dark current only extends 0.2–0.3 V below the built-in potential for PBDTT-DPP:PCBM and PCDTBT:PCBM, because of the presence of the shunt resistance and thus the model should be valid over this range. The P3HT:PCBM cell data cover a larger voltage range and hence the model may lose validity at the lower voltage region of the data. Possibly this effect accounts for the small temperature dependence of $n_{id}kT$ in Fig. 3 and for the curvature in the light intensity dependence of V_{OC} seen in Fig. 7 for P3HT:PCBM, which suggests a decrease in the ideality factor at low light intensity and low voltage.

The SRH model does not require a linear band-edge profile, as was assumed to derive Eq. (10). A curved band edge, for example, arising from space charge, only changes the integral in Eq. (8) because this term contains all the spatial dependence. Hence, the functional form of the dark current would be the same and only the pre-factor would change, and this term only contains terms linear in V and T. For all the devices used herein, however, we measured the amount of dark charge (free plus trapped) residing in the active layer under dark unbiased conditions using the charge extraction by linearly increasing voltage (CELIV) technique and found that in all cases the devices had an undetectable dark-carrier charge density ($< \sim 10^{14-15} \, \text{cm}^{-3}$). The low dark carrier concentration in combination with the low dielectric constants and thin active layers ($\sim 100 \, \text{nm}$) suggest that the Debye length is greater than the device thickness, and therefore the linear band assumption is valid.

B. Verification with numerical drift-diffusion modeling

The analytical model does not consider transport but assumes that carriers can diffuse readily enough across the device to refill traps vacated by recombination events. Hence our model assumes that the opposing drift and diffusion components are much larger than the total current.[23] The flat quasi-Fermi energy approximation breaks down when charge transport cannot replenish traps sufficiently quickly, making

TABLE I. Summary of parameters used in the drift-diffusion simulation. The device thickness was 220 nm and the relative dielectric constant was 3.7. The series (5-7.5 Ω-cm^2) and shunt (3-20 MΩ-cm^2) resistances were tuned to fit the relevant J-V regimes.

Contact Barriers (eV)	Free hole Mobility (cm^2/V-s)	Electron mobility (cm^2/V-s)	N_C, N_V (cm^{-3})	Effect. Band gap (eV)	Total No. of Traps, N_t (cm^{-3})	Hole capture Cross section (cm^2)	Electron capture Cross section (cm^2)	Band tail characteristic Energy, E_0 (meV)	Electron, hole Thermal velocities (cm/s)
0.2	1×10^{-2}	1×10^{-4}	2×10^{20}	1.1	1×10^{19}	5×10^{-14}	1.5×10^{-17}	38	10^6

the hole quasi-Fermi energy bend upward near the cathode contact, which forces recombination to shift toward the anode. For this and general verification reasons, we performed full numerical drift-diffusion modeling to confirm that the model and its associate assumptions are reasonable. The tail-state model outlined in Figure 1(a) was implemented in the SCAPS simulation program,[46] which has been used previously to model polymer:fullerene solar cells.[47] We only considered the polymer HOMO band tail for consistency with the analytic model and because we found that the implementation of a narrower PCBM LUMO band tail had little effect on the properties of interest.

The SCAPS simulator models recombination with the SRH formalism and takes into account band-tail trapped charge in the Poisson equation but does not allow it to contribute to the current. Thus, the SCAPS program implements a transport-energy model where the input drift mobility represents that of a mobile carrier and not the smaller effective value that is often measured in experiments. For this reason, we used a free hole mobility of 1×10^{-2} cm^2/V-s, which is similar to what others have used when implementing such a model for polymer:fullerene solar cells and in good agreement with experimentally measured band mobilities.[36,45,48,49] Because fullerene band tails were ignored, we used an effective mobility of 10^{-4} cm^2/V-s for electrons to take into account that there are LUMO band-tail trap states. However, the magnitude of the electron mobility had little influence on the simulation results. The effective band gap in the model is the interface gap between the polymer HOMO and the fullerene LUMO transport energies, which is about 1.1 eV for P3HT:PCBM.

Simulated dark J-V-T curves using the parameters in Table I are shown in Figure 9(a) and agree well with the experimental P3HT:PCBM data from Figure 1(a). The parameters outlined in Table I are for the case of $T = 295$ K; however, only C_n and the series and shunt resistances were varied slightly over the temperature range in order to fit the data. In general, we found that only the band-tail characteristic energy and the magnitude of the asymmetry of the capture coefficients affected the dark ideality factor in the simulations, which is consistent with our discussions of the analytic model above. A smaller E_0 and/or capture coefficient asymmetry resulted in a steeper slope and therefore lower ideality factor.

The recombination profile at $T = 295$ K and $V = 0.3$ V, in Figure 9(b) confirms that recombination is largest nearer to the cathode contact and therefore in good agreement with the predictions of the analytic model. The reason why the recombination profile does not have a maximum at the cathode, as predicted by our simple analytic model, is due to the

presence of a finite hole diffusion length and a non-zero $C_n n/C_p p$ term in the SRH occupation function, as discussed above. Another factor influencing the temperature dependence of the ideality factor is the decrease in the diffusion constant with decreasing temperature, which will cause the hole qFE to bend upward near the cathode contact and thus force recombination toward the center of the active layer. Despite these details, Figure 9 confirms that the basic approximations made in our model are reasonable. The magnitude of the capture coefficients in the simulations should not be taken as necessarily accurate because they primarily influence the magnitude of the current, but significantly less so the shape, and many other factors of unknown magnitude also influence the magnitude of the current. In addition, the simulation is an effective medium model and does not capture many details of the mechanism and device structure. For
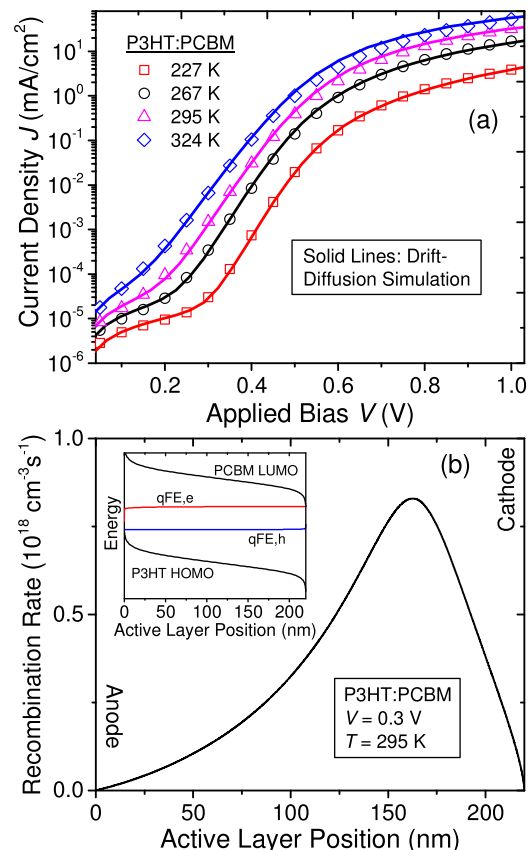

FIG. 9. (a) Experimental J-V-T data for the P3HT:PCBM cell from Fig. 2(a) along with the drift-diffusion simulation results (lines). (b) The recombination rate as a function of position in the active layer corresponding to the simulation in (a) at 295 K and 0.3 V applied bias. The recombination rate has a maximum nearer to the cathode contact. Inset: the associate band diagram with quasi-Fermi energies.

example, the electron capture cross-section is an average over transitions to band-tail states that are spatially distributed at various distances from the interface with transition rates that must vary widely. The local anisotropy of transport in the polymer is also not represented in the model.

VI. SUMMARY AND CONCLUSIONS

A Shockley-Read-Hall analysis to describe the dark forward bias diode current for the case of recombination in an exponential band tail results in the expression for the ideality factor $n_{id} = E_0/kT$, providing a direct link between the dark current and the band-tail slope when band-tail recombination dominates. In two of the three polymers studied and in amorphous silicon, there is excellent agreement between the ideality factor and the measured band tail slope confirming that band tail recombination is the dominant mechanism. In the P3HT:PCBM system, we were able to self-consistently reproduce the measured room temperature ideality factor with both detailed drift-diffusion simulations and our analytical model. The PBDTT-DPP:PCBM cell, on the other hand, has a larger ideality factor than expected from the measured band-tail slope and there is evidence of additional deep states that contribute to a second recombination channel. Other recombination mechanisms can also lead to a different ideality factor from that predicted by the band tail recombination model.

The light intensity dependence of the open-circuit voltage gives an alternative measurement of the dark ideality factor. The dark and light measurements give the same result provided that the voltage dependence of the cell photocurrent is taken into account.

Based on the evidence for recombination through band tail and deep states, further improvement in the organic solar cell efficiency requires materials with a steeper band-tail slope and the ability to suppress the light-induced creation of mid-gap states. Gains in the cell efficiency arise in two ways—a reduction in dark current and an increase in fill factor. Both factors depend exponentially on the band-tail slope, so small changes can make a large difference in the cell efficiency. The band tails reflect the disorder and indicate that more ordered materials are needed. It is interesting to note that the effective mobility of polymer thin film transistors (TFT) has recently increased to about $5\,cm^2/V\text{-}s$ as a result of the introduction of new materials,[50] while the polymer mobility in solar cells is still much smaller. The difference must relate at least partially to a higher degree of molecular ordering in the TFT. If the same level of structural order could be achieved in the cells as in the TFTs, then perhaps the cell efficiency would be substantially increased.

ACKNOWLEDGMENTS

[1]Z. He, C. Zhong, S. Su, M. Xu, H. Wu, and Y. Cao, Nat. Photon. **6**, 591 (2012).

[2]X. Guo, N. Zhou, S. J. Lou, J. Smith, D. B. Tice, J. W. Hennek, R. P. Ortiz, J. T. L. Navarrete, S. Li, J. Strzalka, L. X. Chen, R. P. H. Chang, A. Facchetti, and T. J. Marks, Nat. Photon. **7**, 825 (2013).

[3]J. B. You, L. T. Dou, K. Yoshimura, T. Kato, K. Ohya, T. Moriarty, K. Emery, C.-C. Chen, J. Gao, G. Li, and Y. Yang, Nature Commun. **4**, 1446 (2013).

[4]L. Dou, J. You, Z. Hong, Z. Xu, G. Li, R. A. Street, and Y. Yang, Adv. Mater. **25**, 6642 (2013).

[5]S. A. Hawks, F. Deledalle, J. Yao, D. G. Rebois, G. Li, J. Nelson, Y. Yang, T. Kirchartz, and J. R. Durrant, Adv. Energy Mater. **3**, 1201 (2013).

[6]R. N. Hall, Phys. Rev. **83**, 228 (1951).

[7]W. Shockley and W. T. Read, Phys. Rev. **87**, 835 (1952).

[8]C. T. Sah, R. N. Noyce, and W. Shockley, Proc. Inst. Radio Eng. **45**, 1228 (1957).

[9]G. A. H. Wetzelaer, M. Kuik, M. Lenes, and P. W. M. Blom, Appl. Phys. Lett. **99**, 153506 (2011).

[10]R. A. Street, M. Schoendorf, A. Roy, and J. H. Lee, Phys. Rev. B **81**, 205307 (2010).

[11]L. J. A. Koster, V. D. Mihailetchi, R. Ramaker, and P. W. M. Blom, Appl. Phys. Lett. **86**, 123509 (2005).

[12]T. Kirchartz, F. Deledalle, P. S. Tuladhar, J. R. Durrant, and J. Nelson, J. Phys. Chem. Lett. **4**, 2371 (2013).

[13]T. Kirchartz, B. E. Pieters, J. Kirkpatrick, U. Rau, and J. Nelson, Phys. Rev. B **83**, 115209 (2011).

[14]A. Foertig, J. Rauh, V. Dyakonov, and C. Deibel, Phys. Rev. B **86**, 115302 (2012).

[15]T. Kirchartz and J. Nelson, Phys. Rev. B **86**, 165201 (2012).

[16]R. A. Street, A. Krakaris, and S. R. Cowan, Adv. Funct. Mater. **22**, 4608 (2012).

[17]R. A. Street, J. E. Northrup, and B. S. Krusor, Phys. Rev. B **85**, 205211 (2012).

[18]C. Deibel, A. Wagenpfahl, and V. Dyakonov, Phys. Rev. B **80**, 075203 (2009).

[19]F. Gao, J. Wang, J. C. Blakesley, I. Hwang, Z. Li, and N. C. Greenham, Adv. Energy Mater. **2**, 956 (2012).

[20]C. H. Kim, O. Yaghmazadeh, Y. Bonnassieux, and G. Horowitz, J. Appl. Phys. **110**, 093722 (2011).

[21]L. J. A. Koster, E. C. P. Smits, V. D. Mihailetchi, and P. W. M. Blom, Phys. Rev. B **72**, 085205 (2005).

[22]C. Deibel, A. Wagenpfahl, and V. Dyakonov, Phys. Status Solidi (RRL) **2**, 175 (2008).

[23]N. C. Giebink, G. P. Wiederrecht, M. R. Wasielewski, and S. R. Forrest, Phys. Rev. B **82**, 155305 (2010).

[24]C. van Berkel, M. J. Powell, A. R. Franklin, and I. D. French, J. Appl. Phys. **73**, 5264 (1993).

[25]R. A. Street, K. W. Song, J. E. Northrup, and S. Cowan, Phys. Rev. B **83**, 165207 (2011).

[26]J. C. Blakesley and D. Neher, Phys. Rev. B **84**, 075210 (2011).

[27]L. Tzabari and N. Tessler, J. Appl. Phys. **109**, 064501 (2011).

[28]poly{2,6′-4,8-di(5-ethylhexylthienyl)benzo[1,2-b;3,4-b]dithiophene-alt-5-dibutyloctyl-3,6-bis(5-bromothiophen-2-yl)pyrrolo[3,4-c]pyrrole-1,4-dione}.

[29]G. Li, V. Shrotriya, J. Huang, Y. Yao, T. Moriarty, K. Emery, and Y. Yang, Nature Mater. **4**, 864 (2005).

[30]L. Dou, J. Gao, E. Richard, J. You, C.-C. Chen, K. C. Cha, Y. He, G. Li, and Y. Yang, J. Am. Chem. Soc. **134**, 10071 (2012).

[31]S. H. Park *et al.*, Nat Photon. **3**, 297 (2009).

[32]R. A. Street, P. P. Khlyabich, and B. C. Thompson, Org. Electron. **14**, 2932 (2013).

[33]D. M. Stevens, J. C. Speros, M. A. Hillmyer, and C. D. Frisbie, J. Phys. Chem. C **115**, 20806 (2011).

[34]R. A. Street, Phys. Rev. B **84**, 075208 (2011).

[35]L. Goris, A. Poruba, L. Hod'ákova, M. Vaněček, K. Haenen, M. Nesládek, P. Wagner, D. Vanderzande, L. De Schepper, and J. V. Manca, Appl. Phys. Lett. **88**, 052113 (2006).

[36]R. C. I. MacKenzie, C. G. Shuttle, G. F. Dibb, N. Treat, E. von Hauff, M. J. Robb, C. J. Hawker, M. L. Chabinyc, and J. Nelson, J. Phys. Chem. C **117**, 12407 (2013).

[37]J. Bhattacharya, R. W. Mayer, M. Samiee, and V. L. Dalal, Appl. Phys. Lett. **100**, 193501 (2012).

[38]M. Vanecek, J. Kocka, A. Poruba, and A. Fejfar, J. Appl. Phys. **78**,6203 (1995).

[39]W. B. Jackson and N. M. Amer, Phys. Rev. B **25**, 5559 (1982).

[40]N. F. Mott and E. A. Davis, *Electronic Processes in Non-Crystalline Materials* (Clarendon Press; Oxford University Press, Oxford New York, 1979).

[41]R. A. Street, K. W. Song, and S. Cowan, Org. Electron. **12**, 244 (2011).

[42]R. A. Street, *Hydrogenated Amorphous Silicon* (Cambridge University Press, 1991).

[43]M. Kemerink, J. M. Kramer, H. H. P. Gommans, and R. A. J. Janssen, Appl. Phys. Lett. **88**, 192108 (2006).

[44]D. Rauh, A. Wagenpfahl, C. Deibel, and V. Dyakonov, Appl. Phys. Lett. **98**, 133301 (2011).

[45]R. C. I. MacKenzie, T. Kirchartz, G. F. A. Dibb, and J. Nelson, J. Phys. Chem. C **115**, 9806 (2011).

[46]See http://users.elis.ugent.be/ELISgroups/solar/projects/scaps.html for a description of and access to the SCAPS simulation software.

[47]T. Kirchartz, W. Gong, S. A. Hawks, T. Agostinelli, R. C. I. MacKenzie, Y. Yang, and J. Nelson, J. Phys. Chem. C **116**, 7672 (2012).

[48]M. P. Eng, P. R. F. Barnes, and J. R. Durrant, J. Phys. Chem. Lett. **1**, 3096 (2010).

[49]J. C. Aguirre, C. Arntsen, S. Hernandez, R. Huber, A. M. Nardes, M. Halim1, D. Kilbride, Y. Rubin, S. H. Tolbert, N. Kopidakis, B. J. Schwartz, and D. Neuhauser, Adv. Funct. Mater. **24**, 784 (2014).

[50]J. Li, Y. Zhao, H. S. Tan, Y. Guo, C.-A. Di, G. Yu, Y. Liu, M. Lin, S. H. Lim, Y. Zhou, H. Su, and B. S. Ong, Sci. Rep. **2**, 754 (2012).